Lawrence Berkeley National Laboratory

Title

Amorphous calcium carbonate particles form coral skeletons

Permalink

https://escholarship.org/uc/item/23x6p9f7

Journal

ISSN

Authors

Mass, Tali
Giuffre, Anthony J
Sun, Chang-Yu
et al.

Publication Date

DOI

Peer reviewed

Amorphous calcium carbonate particles form coral skeletons

Tali Mass[a,1], Anthony J. Giuffre[b], Chang-Yu Sun[b], Cayla A. Stifler[b], Matthew J. Frazier[b], Maayan Neder[a,c], Nobumichi Tamura[d], Camelia V. Stan[d], Matthew A. Marcus[d], and Pupa U. P. A. Gilbert[b,e,f,1,2]

[a]Marine Biology Department, University of Haifa, Haifa 31905, Israel; [b]Department of Physics, University of Wisconsin–Madison, Madison, WI 53706; [c]H. Steinitz Marine Biology Laboratory, The Interuniversity Institute of Marine Science, Eilat 88103, Israel; [d]Advanced Light Source, Lawrence Berkeley National Laboratory, Berkeley, CA 94720; [e]Department of Chemistry, University of Wisconsin–Madison, Madison, WI 53706; and [f]Department of Geoscience, University of Wisconsin–Madison, Madison, WI 53706

Do corals form their skeletons by precipitation from solution or by attachment of amorphous precursor particles as observed in other minerals and biominerals? The classical model assumes precipitation in contrast with observed "vital effects," that is, deviations from elemental and isotopic compositions at thermodynamic equilibrium. Here, we show direct spectromicroscopy evidence in *Stylophora pistillata* corals that two amorphous precursors exist, one hydrated and one anhydrous amorphous calcium carbonate (ACC); that these are formed in the tissue as 400-nm particles; and that they attach to the surface of coral skeletons, remain amorphous for hours, and finally, crystallize into aragonite ($CaCO_3$). We show in both coral and synthetic aragonite spherulites that crystal growth by attachment of ACC particles is more than 100 times faster than ion-by-ion growth from solution. Fast growth provides a distinct physiological advantage to corals in the rigors of the reef, a crowded and fiercely competitive ecosystem. Corals are affected by warming-induced bleaching and postmortem dissolution, but the finding here that ACC particles are formed inside tissue may make coral skeleton formation less susceptible to ocean acidification than previously assumed. If this is how other corals form their skeletons, perhaps this is how a few corals survived past CO_2 increases, such as the Paleocene–Eocene Thermal Maximum that occurred 56 Mya.

mesocrystal | PEEM | calcification crisis | vital effects | ocean acidification

The classical model for coral skeleton formation assumes that ions from seawater are either actively or passively (1) transported through the living tissue, they are concentrated (2), and delivered to the growing skeleton surface (3), where they are deposited ion by ion; thus, the coral skeleton should be in equilibrium with bulk seawater (4). Elemental Sr/Ca and Mg/Ca ratios and isotopic $\delta^{11}B$, $\delta^{13}C$, and $\delta^{18}O$ analyses of corals, however, reveal significant deviations from equilibrium, termed "vital effects" (5–8), which cannot be reconciled with the classical model. The alternative is coral formation from amorphous calcium carbonate (ACC) precursor particles formed in the animal tissue, as hypothesized for sea urchins (9), and thus, away from bulk solution and from equilibrium thermodynamics. Why is it important if the coral aragonite crystals form ion by ion from solution or by attachment of amorphous particles?

Coral is one of many marine organisms that biomineralize, that is, form hard crystalline shell or skeletal structures (10). Calcium carbonate ($CaCO_3$) biomineralization is an intensely studied, widespread natural phenomenon, with major implications in paleoclimate reconstructions (11, 12). Coral biomineralization is important to understand how corals responded to past environments (11, 13), thus clarifying their use as paleoenvironmental proxies, their vital effects, and their fate in future changing environments (14). Coral morphology and biomineralization have been studied for decades (15), including the animal tissue and the skeleton that it deposits (16). However, many of the basic mechanisms underlying the aragonite mineral formation remain unknown (1, 17).

ACC in coral was long suspected but never shown (17). Previous experiments aimed at revealing its presence in forming corals did not show evidence of ACC but could not discount it either (18). Three previous lines of evidence suggested that coral skeletons form via amorphous precursors. First, high-resolution scanning electron (19) and atomic force (20) microscopies (SEM and AFM, respectively) revealed that coral skeletons consist of nanoparticles on the order of 100 nm in size. Nanoparticulate texture persisting in mature mineralized tissues has been associated with crystallization by attachment of amorphous particles in vitro (21), in sea urchin spicules (22), and in nacre (23), in contrast with vaterite tunicate spicules, which are not nanoparticulate and likely form ion by ion from solution (24). Second, the spatial distributions of Sr and Mg in coral skeletons are very different from one another, and Mg has been suggested to stabilize ACC (25). Third, crystal growth in vitro in the presence of coral organic matrix showed formation and stabilization of ACC (26). Interestingly, two forms of ACC were observed, with different amounts of water and thermal stability (26, 27). ACC was first identified as a precursor phase in sea urchin spicules (28) and spines (29), larval mollusk shells (30), and a variety of other biominerals. Two different ACC precursor phases were detected on the surface of sea urchin spicules by Politi et al. (31), in their cross-sections by Gong et al. (32), and later, in nacre by DeVol et al. (23).

Significance

Whether coral skeleton crystals grow by attachment of ions from solution or particles from tissue determines (*i*) corals' growth rate, (*ii*) how they survive acidifying oceans, and (*iii*) the isotopes in the crystals used for reconstructing ancient temperatures. Our data show that two amorphous precursors exist, one hydrated and one dehydrated amorphous calcium carbonate; that these are formed in the tissue as ~400-nm particles; and that they attach to the surface of coral skeletons, remain amorphous for hours, and finally crystallize into aragonite. Since these particles are formed inside tissue, coral skeleton growth may be less susceptible to ocean acidification than previously assumed. Coral bleaching and postmortem dissolution of the skeleton will occur, but a calcification crisis may not.

Can amorphous precursors be observed during coral formation? We addressed this question using photoemission electron spectromicroscopy (PEEM) and X-ray absorption near-edge structure spectroscopy with 20-nm resolution (23) to directly observe all mineral phases present in adult coral and newly settled spat skeletons, all freshly killed. We found clear spectroscopic evidence of two amorphous precursor phases, hydrated amorphous calcium carbonate (ACC-H_2O) and anhydrous ACC, present only at the newly deposited surface of growing coral skeletons, at the centers of calcification (CoCs), and in particles that appear to be within the tissue near the growing surface.

Results and Discussion

In Figs. 1–4, we present direct evidence of amorphous precursor phases in fresh, forming coral skeletons of *Stylophora pistillata* in various developmental stages and coral locations. Figs. 1–4 show "component maps" obtained from PEEM data by fitting each single-pixel spectrum with a linear combination of spectral "components," displayed in Fig. 1A, and assigning to that pixel a color, which displays quantitatively the proportion of each component. The same region, at the interface of tissue and coral skeleton, is also shown in visible light microscopy in Figs. S1 and S2.
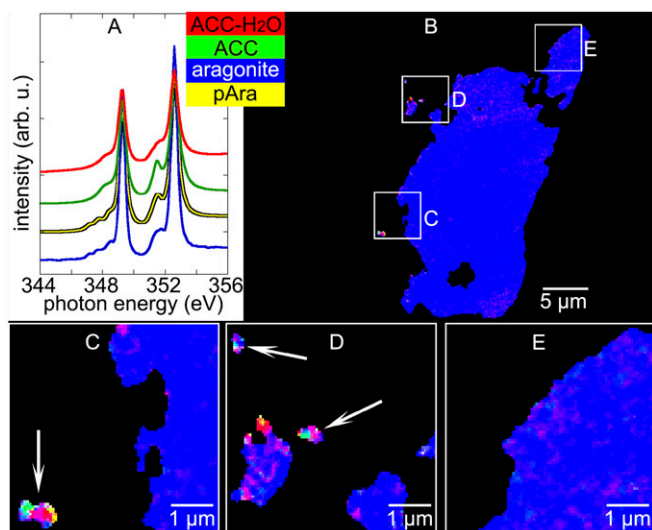

Fig. 1. Component spectra and component maps of tissue and fresh, forming coral skeleton in a spine that appears separate from the rest of the skeleton, as it is curved and incompletely exposed in this polished surface. These data were acquired 25 h postmortem. (A) The reference Ca spectra used as components in all component maps in this work. (B) Component map of forming coral at the tissue–skeleton interface in *S. pistillata*. In a component map, colors indicate mineral phases, as distinguished by their spectra in A, and are correspondingly colored. In A–E, blue pixels are mostly or completely aragonite; ACC-H_2O, ACC, and pAra are displayed in red, green, and yellow, respectively. (C–E) Magnified component maps from the correspondingly labeled boxes in B. C and D show three particles (arrows) surrounded by tissue, which clearly contain more ACC-H_2O, ACC, and pAra pixels than any other region in this work. In the forming coral skeleton, instead, there are only ACC-H_2O and aragonite, very little ACC, and no pAra at all, as shown in E. The spectra in A are normalized to have the same area under the curve between 345 and 355 eV. They are vertically displaced here for clarity, not during component mapping. The maps in B–E were obtained from a stack of PEEM images, fitting every pixel with a linear combination of the four component spectra in A and displaying in each pixel the proportion of each spectrum that best fits the spectrum of that pixel in red, green, blue, and yellow colors. Since yellow never occurs as a mixture of red and green, displaying pAra as yellow is unambiguous (Figs. S8 and S9). Important additional data for this region are in Figs. S1–S3, S8, and S9, and repeat component maps are in Fig. S3. Quantitative analysis for the abundance of each mineral phase is presented in Table 1.
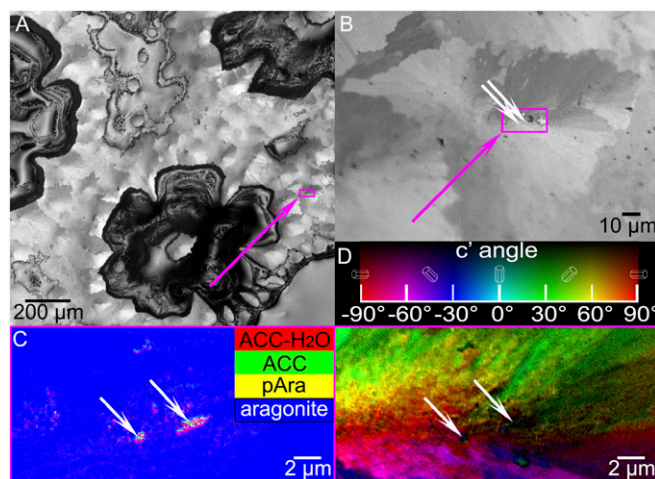

Fig. 2. CoCs in a more mature part of the coral skeleton. (A) Visible light microscopy image obtained with crossed polarizers. In A and B, the magenta boxes indicate the region magnified in C and D. (B) Zoomed in cross-polarizer micrograph showing crystals that radiate out of the CoCs. (C) Zoomed in component map showing abundant ACC-H_2O, ACC, and pAra in the CoCs, indicated by the white arrows. The repeat component map for this region is in Fig. S3. (D) PIC map of the same CoCs shown in B, with white arrows in precisely the same positions. Notice that, where the amorphous precursors are localized in C, this PIC map shows no crystallinity; that is, no polarization dependence, displayed as black pixels.

The forming coral skeleton in Fig. 1 is as fresh as possible (25 h postmortem). It contains a remarkable amount of ACC-H_2O: more than 20% of the pixels contain at least some ACC-H_2O (as shown in Table 1) and are, therefore, red or magenta pixels interspersed with aragonite. The observation of red or magenta pixels is consistent across various skeletal locations: a growing spine in adult coral (Fig. 1 B and E), one in a settled and calcifying spat (Fig. 3), and a growing septum in a corallite of an adult coral (Fig. 4). Very little ACC is observed (~2% green pixels in adult and ~10% in the spat skeletons). This differs from what was observed in sea urchin spicules (32) and nacre (23), where the most abundant amorphous phase observed was anhydrous ACC, not ACC-H_2O as observed here.

Most interestingly, since in Fig. 1B, both the coral tissue and the growing coral skeleton are imaged, we captured three mineral particles surrounded by tissue (Figs. S1 and S2) with spectra that show mostly ACC-H_2O (63%) but also, ACC (20%) and poorly crystalline aragonite (pAra; 12%) (Table 1). These three particles, magnified in Fig. 1 C and D, are surprisingly large [0.4 ± 0.2 μm in size (median $\pm$ SD)] and could be in the skeleton in structures above or below the image plane. Based on the fact that they contain so much more ACC-H_2O, ACC, and pAra than is ever found in any skeletal elements (Table 1), however, we deduce that they must be in tissue. Synthetic ACC-H_2O crystallizes readily, especially in contact with water. Thus, the observation of long-lived ACC-H_2O implies inhibition of the transition from ACC-H_2O to ACC in the tissue and in the growing coral skeleton. Because repeat acquisitions show some of the ACC-H_2O transformed into ACC as a consequence of radiation damage (Fig. S3), we presume that this thermodynamically downhill transition (33) is accelerated by radiation exposure but would happen spontaneously in the undisturbed coral. In the particles within the tissue regions, we observe greater concentrations of ACC than in the forming coral skeleton, suggesting that this phase is stabilized in the tissue but not in the skeleton, where it is extremely short-lived. Greater stabilization of ACC in tissue is consistent with preventing crystallization more in the tissue (that is, at the wrong time and place) than in the skeleton, which makes sense.
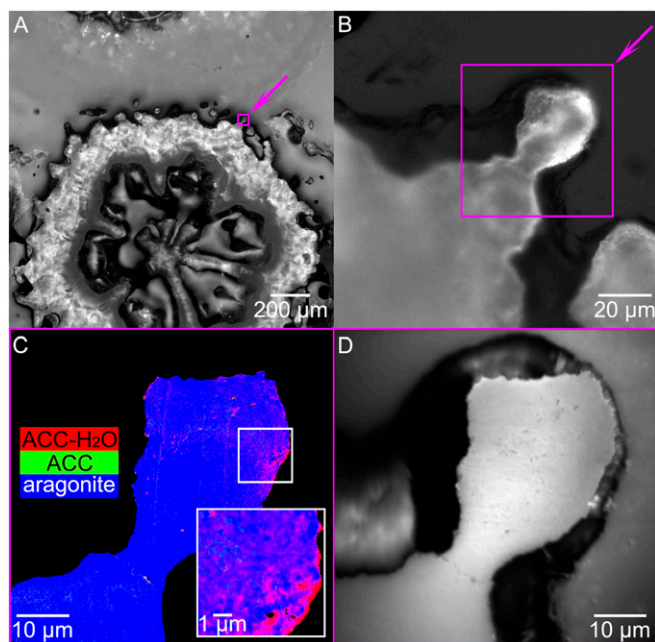
Fig. 3. Amorphous precursor phases in a forming spine in a 2-wk-old spat (that is, a coral larva right after it settled and started forming a skeleton). These data were acquired 28 h postmortem. ACC-H_2O is abundant, ACC is sparse, and pAra is absent from all skeleton regions (spat here, adult in Figs. 1 and 4), except for the CoCs (Fig. 2). (*A* and *B*) Cross-polarizer micrographs of a spat spine, with magenta arrows and boxes indicating the area magnified in *C* and *D*. (*C*) Component map obtained with the same four reference spectra as in all other data in this work, although here, we omitted the pAra label to stress that we found no pAra. *C, Inset* shows a zoomed in map for the white box region. (*D*) Average of 121 stacked PEEM images (termed movie), from which the component map in *C* was obtained. The repeat component map for this region is in Fig. S3, and quantitative phase analysis is in Table 1.

Can dissolution of ACC-H_2O and reprecipitation as aragonite at the biomineral formation site occur, instead of solid-state transformation from ACC to crystal? Based on the paucity of ACC observed in all coral skeletons [<10% of pixels have any ACC in the coral skeleton (Table 1), and even in those pixels, ACC is never pure but 80% ACC at most], dissolution of ACC-H_2O or direct precipitation from solution is possible. However, this cannot be the only phenomenon occurring, as that would imply complete absence of ACC, which was never observed in any areas of forming coral skeletons (Table 1). The existence of some ACC leads to the conclusion that only or mostly solid-state transformations occur from ACC-H_2O to ACC to aragonite.

A pAra phase was previously observed in coral. This spectrum is similar to aragonite around 348 eV (peak 4 in Fig. S4) and to ACC around 351.5 eV (peak 2 in Fig. S4); hence, it was previously assigned to a protoaragonite or poorly crystalline aragonite mineral (23). With the normalization used in Fig. S4, it is clear that pAra has a much more intense peak 1, and thus, it is a crystalline phase, far more ordered than ACC or ACC-H_2O but less ordered than aragonite. It is certainly not a mixture of ACC and aragonite (23); thus, it can only be a poorly crystalline aragonite phase. The disorder may be caused by, for example, incorporation of organic molecules in the crystal (34). The pAra mineral was previously observed in the CoCs of a 10-y-old *Madracis* coral (23). Here, we confirmed this observation in *S. pistillata*, finding abundant pAra localized in the CoCs, as shown in Fig. 2*C*, and not anywhere else in the coral skeletons (Figs. 3 and 4). Interestingly, the pAra phase was also observed in the tissue particles in Fig. 1. Thus, the pAra phase, stabilized in the

living tissue, is delivered and remains stabilized in the skeleton but only in the CoCs, where it persists for years. This is consistent with observations of CoC-specific organic molecules by Cuif et al. (35) and Mass et al. (20) and with the observation of Mg in CoCs (25, 36). Since the pAra phase in CoCs was never observed in either *Stylophora* or *Madracis* (23) to crystallize to aragonite, we conclude that it cannot be an "immature aragonite" or "ACC" phase as proposed by Von Euw et al. (36), nor one of the "polyamorphous" precursor phases described by Cartwright et al. (37), or the "protoaragonite" described by Farhadi-Khouzani et al. (38). The pAra phase in CoCs is stable or stabilized poorly crystalline aragonite.

Our data show that the pAra particles found in the CoCs were already pAra in the tissue (Fig. 1); thus, there is no evidence of nucleation events in the CoCs, as was proposed by Von Euw et al. (36).

The other ACC-H_2O and ACC phases do not exhibit any of the spectral features characteristic of aragonite (peaks 2 and 4 in Fig. S4); thus, they cannot be considered protoaragonite phases (37, 38). They are spectroscopically similar to those detected in forming calcite biominerals (31, 32, 39); thus, they could be termed "protocalcite" phases.

Additional evidence that the precursor phases ACC-H_2O and ACC observed in forming coral or the CoCs are indeed amorphous is provided by polarization-dependent imaging contrast (PIC) mapping, which displays in different colors the orientation of crystalline *c* axes in carbonate crystals (40, 41). The PIC map in Fig. 2*D*, for example, shows that, where pixels are red or green in the component map (Fig. 2*C*), they are black in the PIC map
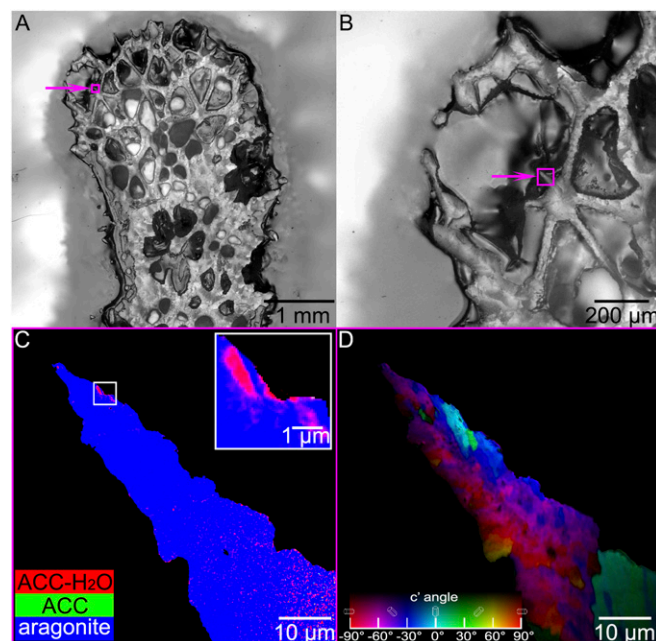

Fig. 4. Amorphous precursors in a growing coral septum. These data were acquired 31 h postmortem. (*A* and *B*) Cross-polarizer micrographs, with magenta arrows and boxes showing the region magnified in *C* and *D*. (*A*) The whole coral branch, termed nubbin. (*B*) A flower-shaped holey structure termed corallite, with four fully formed and two forming septa. (*C*) Component map of a forming septum, showing that, in this adult coral, the forming skeleton has a lot of ACC-H_2O, very little ACC, and almost no pAra. (*D*) PIC map showing aragonite crystals in the septum, distinguished by different colors, which quantitatively identify their crystal orientations. By the time that the PIC map was acquired (32 h postmortem), all of the amorphous precursor phases had already crystallized to aragonite because of time delay and radiation damage. The repeat component map for this region, acquired immediately after the first and before PIC mapping, is in Fig. S3, and quantitative phase analysis is in Table 1.

Table 1. Occurrence of red (R), green (G), blue (B), and yellow (Y) pixels in each component map

Figure	R pixels (%)	G pixels (%)	B pixels (%)	Y pixels (%)
Fig. 1, coral skeleton only	21	2	100	0
Fig. 1, particles appearing in coral tissue only	63	20	98	12
Fig. 1	22	2	100	0
Fig. 2	15	6	100	1
Fig. 3	25	10	100	2
Fig. 4	16	1	98	1

Percentages of each phase [ACC-H_2O, red (R); ACC, green (G); aragonite, blue (B); and pAra, yellow (Y)] in the nonblack pixels present in each of Figs. 1–4 and Fig. S9. Notice the paucity of ACC and pAra compared with ACC-H_2O and the abundance of aragonite everywhere, even in the pixels where either ACC or ACC-H_2O was detected. Analyzing only the particles in the tissue in Fig. 1, significantly greater abundance of ACC-H_2O, ACC, and pAra was observed. The pixels counted in each R, G, B, and Y map were those with at least 5% of the relevant phase. For example, if a pixel contained 10% ACC-H_2O, 10% ACC, 70% aragonite, and 10% pAra, it was counted as one pixel in each color map; thus, the total percentages are greater than 100%. Fig. S9 shows the spatial distribution of these pixels.

(Fig. 2D), confirming lack of crystallinity. White arrows in Fig. 2 C and D point precisely at the same CoC locations in the two maps, and these appear rich in amorphous phases in the component map and mostly black in the PIC map. Black in a PIC map may also indicate orientation: aragonite crystals or nanocrystals with their c axes pointing into the beam appear black (e.g., near the scale bar in Fig. 2D). The colocalization of amorphous spectra and black pixels in the PIC map (Fig. 2 C and D, respectively) make the interpretation of black in the PIC map unambiguous. Amorphous regions in Figs. 3 and 4 had already crystallized by the time that PIC maps were acquired.

Can the large amorphous particles identified in fixed and embedded tissue regions in Fig. 1 be detected in living corals? Confocal microscopy data in Fig. 5 show that this is indeed possible. The blue calcein-stained particles, outlined in Fig. 5D, vary in size between 0.4 and 9.4 µm, with 400 ± 700 nm being both the median and the mode $\pm$ SD, in the forming mineral (FM) and in the living tissue (LT). The LT has some particles greater than 1 µm, as previously observed (42) and as seen in Fig. 1C. The 400-nm most frequent particle size in LT is in agreement with that observed in Fig. 1 and in some FM regions in Figs. 2–4; therefore, it must be correct. It also coincides with the size of type I vesicles Clode and Marshall observed to be the most abundant in calcifying cells near the FM after cryofracturing them (43), but it is considerably larger than the 100 nm expected from SEM observations of coral skeletons (19–21, 44).

In Fig. 6, we show particles identified by their crystal orientations in PIC maps of both a natural coral skeleton and a synthetic aragonite spherulite grown in vitro by particle attachment. Fig. S5A shows 400-nm particles, and Fig. S5B shows that crystal orientation domains have edges with diameter of curvature ~400 nm, consistent with attachment of particles of this size. In Figs. 3 and 4, amorphous domains are also on the order of 400 nm in the forming skeleton, again confirming that such large particles originating in LT are not unreasonable.

Monochromatic microdiffraction of two *S. pistillata* mature skeletons finds coherence lengths in different locations of 250 nm in the CoCs and 300 nm in the large crystalline domain areas. These are the minima observed; the maxima, averages of all data, and their errors are presented in *SI Materials and Methods*. These coherence length minima are similar to the smallest particle size observed in PIC maps and confocal microscopy in those same regions. Where a larger coherence length is observed in the large

domain areas, uniformly colored in PIC maps, the particles need not necessarily have been larger; it is possible that multiple 400-nm particles became perfectly cooriented as they crystallized in those locations. In SEM images of coral skeletons, we see particle sizes varying between 100 nm and more than 1 micron (Fig. S6 E–H), consistent with this interpretation.

All of these data combined present direct experimental evidence that the coral skeleton indeed forms by attachment of amorphous precursor particles as previously hypothesized but never directly observed; that these are ACC-H_2O and anhydrous ACC; and that, after they crystallize to aragonite, the particles may retain distinct orientations. This implies that the biomineral is not formed in equilibrium with a large body of water but under direct biological control inside the tissue and behind tightly sealed membranes, as summarized in the model of Fig. 7 and described below.

Model for CaCO₃ Biomineralization via Amorphous Precursor Particles. A model for calcium carbonate biomineral formation via amorphous precursor particles is presented in Fig. 7. This is based, in part, on these data and in part, on previous work, and it encompasses all that is currently known about this highly investigated topic to the best of our knowledge.

Marine biomineral crystal formation takes place in five steps.

i) Seawater is rich in Ca^{2+} ions but also, Mg^{2+}, Sr^{2+}, bicarbonate, a few carbonate, and many other ions, all of which are omitted from Fig. 7 for clarity. Seawater is captured by endocytosis, that is, a process in which the cell membrane invaginates, such that the external seawater is incorporated into an intracellular vesicle (on the left in Fig. 7). This is consistent with movies presented by Erez and Braun (45), in which calcein-stained Ca
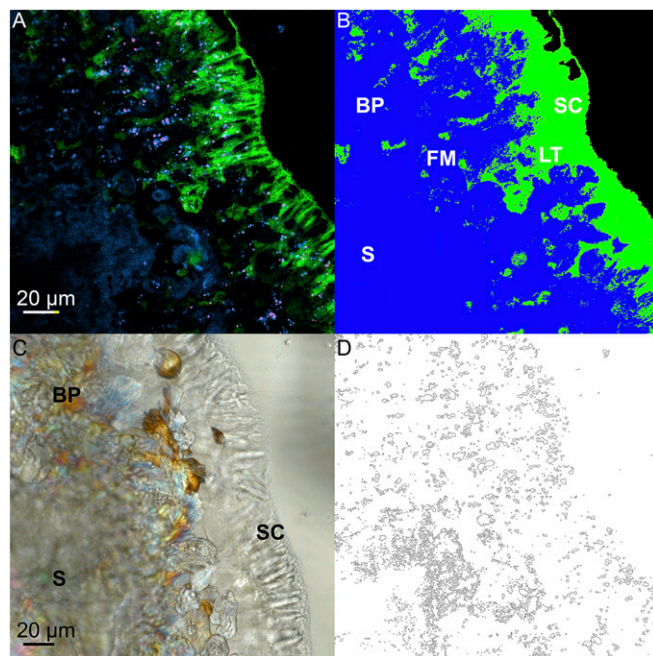

Fig. 5. (*A*) Confocal micrograph of a living spat. Calcein fluorescence is displayed in blue; native green fluorescent protein (GFP) and chlorophyll are in green and red, respectively. (*B*) Map of the same spat, where regions of FM and LT are filled with blue and green, respectively. Notice that they are interspersed, with LT in FM and FM in LT. (*C*) Differential interference contrast micrograph acquired with crossed polarizers, showing a similar region of the same spat, where a basal plate (BP), a growing septum (S), and a layer of stinging cells (SC) are better recognizable, and therefore, they could be placed in *B*. (*D*) Outlines of all 2,726 blue-stained particles analyzed, which vary in size between 0.4 and 9.4 µm.
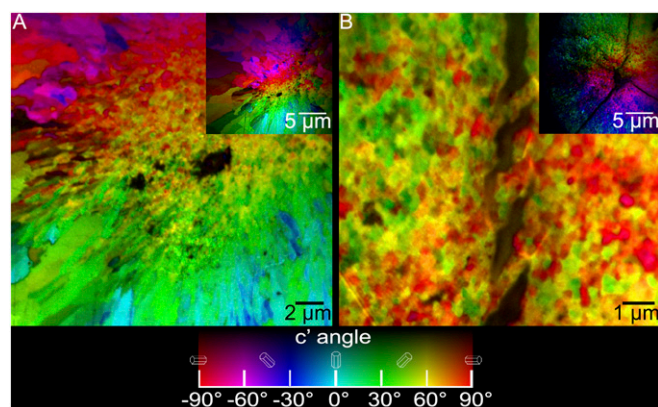
Fig. 6. PIC maps showing nanoparticles with different orientations (*A*) at and around CoCs in an *S. pistillata* coral skeleton and (*B*) in synthetic aragonite spherulite grown via particle attachment. *Insets* show lower magnification PIC maps of the same regions in *A* and *B*. Crack bridging in *B* provides additional evidence that the spherulite is formed by particles. Fig. S5 has details on particle sizes in *A* and *B*.

in seawater enters the cells in vesicles and is ultimately incorporated into the growing coral. Additional strong evidence by Tambutté et al. (46) supports this statement in coral, by Khalifa et al. (47) supports this statement in foraminifera, and by Vidavsky (9) supports this statement in sea urchin embryos. The biomineral-forming cells are calicoblastic cells in coral, primary mesenchyme cells in sea urchins, endothelial cells in the mantle of shell-forming mollusks, and the only possible cell in single-cell foraminifera. These are the cells in immediate contact with the deposited mineral (48). If seawater was incorporated by other cells at the surface of a larger, more complex organism, such as coral polyp or a whole-sea urchin embryo, and therefore, far away from these cells, then the vesicle may have been transferred from cell to cell across a variety of tissues. We show only one unstructured tissue in Fig. 7 for simplicity. The color gradient is purely ornamental, not meant to indicate anything.

ii) ACC particles are gradually formed in the vesicle. This implies the addition of CO_3^{2-} ions and the stabilization of amorphous precursor phases, which would otherwise transform into crystals instantaneously but are found to be stable for up to 32 h in this paper, both in the tissue (Fig. 1 *C* and *D*) and in the growing biomineral (Figs. 1 *B, C,* and *E* and 2–4). We note that, in this work, we see mineral particles in the tissue, both in component maps and in confocal microscopy. These are surprisingly large [400 nm as observed in both methods, once in the fixed (Fig. 1 *C* and *D*) and once in the LT (Fig. 5 *A* and *D*)], but we cannot say that mineral is localized in vesicles. Previous work by Clode and Marshall (43) showed that 400-nm vesicles were the most abundant objects observed inside cells immediately adjacent to the growing skeleton, when the cells were cryofractured and imaged by cryo-SEM (44). Venn et al. (42) observe half-micrometer mineral particles in coral LT near the skeleton. We, therefore, deduce that all of these separate observations refer to the same objects: ~400-nm vesicles, delivering ACC to the FM skeleton. Mass et al. (20) used immunolocalization to show that acidic proteins are indeed present in the coral skeleton, as expected, but also throughout the coral tissue layers. Reggi et al. (26) and Falini et al. (27) showed that the organic matrix proteins extracted from coral skeletons stabilize ACC in vitro in the absence of cells. ACC stabilization by proteins was also observed in sea urchin spicules (32) and in fish intestines (49). These proteins, therefore, may be in the same vesicles as ACC.

iii) The carbonate ions are injected into the vesicle one at a time by an active multicomponent biological pathway that remains to be elucidated. Zoccola et al. (50) showed that, in coral, bicarbonate transporters deliver HCO_3^- to the calcification site

and may, therefore, be one component of this transport into vesicles pathway. The vesicles may be the site where the calcifying fluid studied by Comeau et al. (51) resides. Vidavsky et al. (52) showed that, in sea urchin embryos, intracellular vesicles contain the mineral that will ultimately form the spicule. In our model, the vesicle, initially containing only seawater, gradually and actively is injected with carbonate ions; thus, ion pairs of $CaCO_3$ form (second, third, and fourth vesicles in Fig. 7). After enough Ca^{2+} ions are paired with carbonate ions, an amorphous hydrated form of calcium carbonate aggregates (fifth vesicle at the bottom in Fig. 7).

iv) The vesicle containing amorphous precursors is ultimately transported toward the cell membrane near the biomineral, and its ACC content is ejected by exocytosis. Thus, it is deposited directly on the growing surface of the biomineral, which is in immediate contact with the cell (or cell processes, as in sea urchin embryos) (9, 52, 53). At this point, deposited particles are still amorphous and, at least in part, hydrated. They then attach to one another and fill space (54). Memory of particle attachment is retained in the mature biominerals, which cryofracture in liquid nitrogen with a granular fracture surface in sea urchin spicules (22), mollusk shell nacre (23), and coral skeletons (20) but not in ascidian vaterite spicules that likely grow ion by ion from solution and present a smooth cryofracture figure at the nanoscale (24).
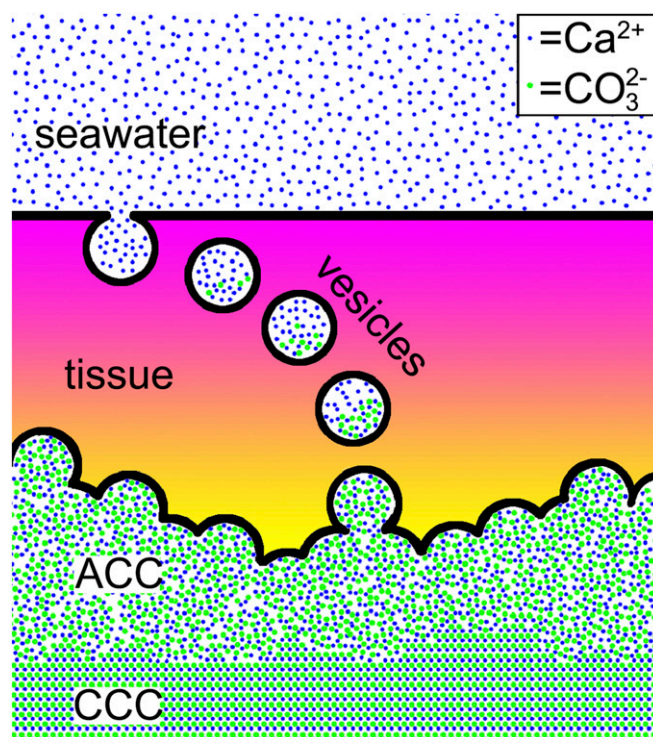

Fig. 7. Model for the formation of coral skeleton or other calcium carbonate marine biomineral. Divalent cations, mostly Ca^{2+} but also, Mg^{2+}, and Sr^{2+} ions are represented as blue dots at all stages of biomineral crystal formation, which takes place in five steps (*i–v*) as described in the text. The carbonate ions $–CO_3^{2-}$, which originate from within the LT, are represented by green dots here. LT separates seawater from the growing biomineral; thus, as long as the animal is alive, the biomineral is not exposed to seawater and will not dissolve, even at low pH. Abiotic overgrowth is also excluded. Seawater is endocytosed (in the upper left) into vesicles and enriched in carbonate ions, and therefore, ACC-H_2O and anhydrous ACC precursors are precipitated and stabilized in these vesicles. The vesicles are transported to the side of the tissue in immediate contact with the growing biomineral surface, and their ACC content is exocytosed there. After a day or so, all of the ACC transforms into CCC. CCC is aragonite in coral or nacre and calcite in foraminifera or sea urchin spines, spicules, or teeth.

v) After a day or so, most or all of the ACC-H_2O transformed into ACC and then, into crystalline calcium carbonate (CCC) as shown by the ordered pattern at the bottom of Fig. 7. The ACC-H_2O, ACC, and CCC phases are progressively more stable and thus, energetically downhill (23, 32, 33). The pAra phase has not been characterized energetically, as it is impossible to isolate. Based on peak 1 amplitude at the Ca L-edge (Fig. 1*A* and Fig. S4), however, we deduce that this phase is more ordered than ACC and less so than aragonite. It is not at all clear, however, that this phase will ever transform into aragonite (23); hence, it cannot be a proto- or a precursor phase (38). In *Madracis* corals, it does not transform into fully crystalline aragonite in the CoCs, even after a decade (23). One possibility is that this poorly crystalline form of aragonite is disordered by occluded organics (34). In coral and other biominerals, there may be concomitant partial dissolution and reprecipitation, as shown in vitro by Gal et al. (21), but in sea urchin spicules, there is only direct solid-state transformation of ACC into calcite as shown by extensive anhydrous ACC regions in direct contact with calcite in sea urchin spicules (32). In coral skeletons, the anhydrous ACC phase is much more sporadically observed; thus, we conclude that this phase is short-lived (Fig. S7*B*).

We now discuss this model.

In biological systems, such as coral, myriad genetic, biochemical, or metabolic complications exist and could, therefore, be included, but they would not help convey a few key ideas; thus, we omit them from this model of $CaCO_3$ assembly by particle attachment. One key feature that this model describes is that of the separate origins of metal and carbonate ions, which is key to reconciling and explaining extensive and apparently contradictory results on isotopic compositions.

Metal Ions. The fact that, in the model of Fig. 7, seawater provides the metal ions Ca^{2+}, Mg^{2+}, and Sr^{2+} satisfactorily explains why the elemental ratios Sr^{2+}/Ca^{2+} and Mg^{2+}/Ca^{2+} in corals, both modern and fossil, so faithfully represent the environmental temperature. Beautiful data by Beck et al. showed this first (11), and many others followed, including Schrag and Linsley (55). There are deviations from environmental parameters termed vital effects on Sr^{2+}/Ca^{2+} and Mg^{2+}/Ca^{2+} ratios (56), which various groups ascribed to photosynthesis by the zooxanthellae (6, 57), pH (42, 58), location in the coral (7, 59), or Rayleigh fractionation (60, 61), but when Sr^{2+}/Ca^{2+} and Mg^{2+}/Ca^{2+} ratios work as temperature proxies, they work extremely well; thus, they cannot be ignored. Ca^{2+}, Mg^{2+}, and Sr^{2+} ions must come from seawater, and when $CaCO_3$ first assembles in the vesicle, it must be in the presence of at least a few Mg^{2+} and Sr^{2+} ions for their T-dependent incorporation into the biomineral.

Carbonate Ions. Many authors lament over vital effects (5, 62) on isotopic ratios $\delta^{18}O$ and $\delta^{13}C$ in coral, but Adkins et al. (7) showed magnificent data on $\delta^{18}O$ and $\delta^{13}C$, which strongly cor-relate with one another. Again, when these isotopic ratios work, they work extremely well; thus, we propose a possible explanation: C and O are both part of the carbonate $-CO_3^{2-}$ ion, which in our model, is formed in the tissue and by the organism, not from atmospheric CO_2, $-HCO_3^-$, or $-CO_3^{2-}$ from seawater.

Since both C and O result from biological functions, any parameter affecting C also affects O in the same direction and by the same amount. This is also in agreement with Spero et al. (63), who showed that that C and O isotopes covary with carbonate ion concentration and hence, with each other, providing a simple explanation for $\delta^{18}O$ and $\delta^{13}C$ data, which is source-independent. It is possible that the coral of Adkins et al. (7) is simpler, because it is a deep sea coral without photosynthetic symbionts, and photo-synthesis has been shown to strongly affect $\delta^{13}C$ values in coral (6). The major source of carbonate ions is metabolic CO_2 (15, 64, 65), and bicarbonate may exit the cells via a bicarbonate transporter (50), whereas Ca^{2+} ion transport is dependent of voltage-gated calcium channels (66). A schematic summarizing ion transport, physiological, and molecular components of coral biomineralization was presented by Bhattacharya et al. (ref. 67, figure 2).

Metal and Carbonate Ions Have Distinct Origins. The key point of our model is that the metal ions and the carbonate ions have completely different origins, are processed independently, and therefore, show inconsistent behavior, previously assumed to be a problem if one wants to use coral skeletons to measure paleoenvironmental temperatures. In fossils, one of the few if not the only way to validate temperatures measured by Sr^{2+}/Ca^{2+} ratios is to compare them with temperatures measured by $\delta^{18}O$ or the clumped isotope thermometer (68). Such comparisons may be extremely successful, as in the work by Ghosh et al. (68), but they also frequently fail. The model that we propose here predicts that the metal and the carbonate origins are different; thus, they should not behave similarly universally. In addition, when ACC is formed in intracellular vesicles, as shown here, the metal ratios may also be altered by small organic molecules, as observed in vitro for Mg^{2+}/Ca^{2+} ratios by Dove and coworkers (69), or by deposition rates as shown in coccolithophorids and foraminifera (70, 71). Some of the vital effects, that is, deviations of elemental and isotopic compositions predicted by thermodynamics and environmental parameters alone, observed in corals (7, 48, 59, 60) may be reinterpreted in the light of the data and model presented here for coral formation via attachment of amorphous particles, in direct contrast with the previously assumed precipitation of coral minerals ion by ion from solution.

Selection of Phase. One might ask why ACC-H_2O is produced rather than more stable phases, such as aragonite. It is actually common in natural systems that the least stable phase that is energetically available is the one that forms first. This observation is known as the Ostwald Step Rule or the Gay–Lussac–Ostwald Step Rule (72, 73). The high supersaturation produced

Table 2. Abiotic aragonite ion-by-ion growth rate

Study	p (μm/d)	n	r (μm/d) at $S = 3.695$	T (°C)	pH	Other notes
Burton and Walter, 1987 (82)	0.033	1.70	0.18	25	NA	Salinity 35, filtered Gulf Stream water
Mucci et al., 1989 (83)	0.030	2.20	0.27	25	7.53–7.70	ASW without sulfate
Mucci et al., 1989 (83)	0.019	1.60	0.09	25	7.60–7.94	ASW with sulfate
Zhong and Mucci, 1989 (84)	0.011	2.26	0.10	25	7.48–7.67	ASW, salinity 35–44
Gutjahr et al., 1996 (85)	0.165	1.05	0.47	20	7.91	ASW
Average of all growth rates			0.22			

Abiotic aragonite ion-by-ion growth rate measured by various authors. The rate constant p and reaction order n were measured in abiotic aragonite precipitation experiments in seawater and artificial seawater (ASW). Here, we calculate the growth rate r at the seawater saturation with respect to aragonite of 3.695. Additional experimental conditions that may account for differences between studies, such as temperature, pH, and salinity, are also shown here. NA, not available.

Table 3. Biogenic aragonite particle-by-particle growth rate

Study	S. pistillata linear growth rate (various units)	S. pistillata growth rate (mm/y)	S. pistillata growth rate (μm/d)
Liberman et al., 1995 (ref. 86, figure 2)	0.5–2.0 cm in 7 mo	8.6–34.3	24–94
Kotb, 2001 at 5-m depth (87)	9.24 mm/y	9.24	25
Shaish et al., 2006, Bal in table 1 in ref. 88	7.6–13.3 mm/y	7.6–13.3	21–36
Average of all growth rates			40

S. pistillata linear growth rate measured by various authors.

by the injection of carbonate ions into the vesicle provides the energy needed to produce the less stable phase. We acknowledge that the Ostwald Step Rule only considers classical ion-by-ion pathways of nucleation and growth (73) and that much remains to be learned about the processes involved in crystallization by attachment of amorphous particles (22).

Particle Attachment. The particle attachment mechanism described here is quite different from the oriented attachment of crystalline particles described by Penn and Banfield (74) in synthetic biomineral systems, Banfield et al. (75) in bacterial biomineral systems, and Cölfen and Antonietti (76, 77) in the formation of a variety of mesocrystals. In oriented attachment, nanoparticles are crystalline first, and then, they attach to one another, whereas in coral skeletons, nanoparticles are initially amorphous; then, they attach and fill space, and hours later, they crystallize.

What is the advantage to the animal of formation by attachment of amorphous particles as opposed to precipitation from solution? One hypothesis explored here involves aragonite growth rate. Corals with fast-growing skeletons outcompete their neighbors in crowded reefs by reaching farther for better illumination, exposure to nutrients, and disposal of waste or for faster regeneration after damage by tropical storms or predators (78). Thus, fast growth must be a terrific physiological advantage for the coral polyps and the symbiont zooxanthellae in the rigors of crowded and competitive reef ecosystems.

How do growth rates by attachment of ions or ACC particles compare? Aragonite growth experiments in the laboratory using realistic seawater pH, temperature, and concentrations show an average linear growth rate of 0.22 μm/d (Table 2). S. pistillata, the coral used here, elongates its skeleton an average of 40 μm/d (Table 3), thus more than 100 times faster than it would if its aragonite precipitated ion by ion from solution.

Is this astounding growth rate achieved biochemically, or is it an abiotic phenomenon? To tackle this question, we grew synthetic aragonite spherulites, which form by attachment of nanoparticles in vitro as shown in Fig. 6B and Fig. S6 in the absence of any organic molecules, and measured their growth rates, as presented in Table 4. Again, the growth rate is at least 100 times greater than for ion by ion growth. We, therefore, conclude that it is growth via ACC particle attachment that enables fast aragonite crystal growth. Biochemical growth modifiers may also play a significant role in coral skeleton growth rate, but in vitro particle-by-particle growth significantly increases growth rate compared with ion-by-ion growth and does so in the

absence of any organic molecules. (Biological control is still all important in forming, stabilizing, and delivering ACC particles to the growing biomineral!)

Coral skeletons formed via attachment of amorphous particles retain a nanoparticulate texture even years after formation, as is visible in PIC maps (Fig. 6A) and also by SEM of cryofractured coral skeleton (Fig. S6) but not in geologic aragonite (Fig. S6). Other authors saw ~100-nm particles with SEM or AFM in corals (19, 20), as do we in Fig. S6 E–H along with other ~400-nm or larger features. This reinforces the well-established notion (22) that morphology alone cannot provide accurate measurement of particle sizes, but combined with PIC mapping and component mapping, it provides a more complete and therefore, stronger case for coral crystallization by particle attachment. There may also exist concomitant ion-by-ion precipitation, but granular structure in SEM, in crystal orientation PIC maps, and in direct observation of particles in the tissue all concur to show that particle attachment plays a major role in coral skeleton formation. Even slow-growing corals in the slowest growth conditions of low light (79) still grow faster than ion-by-ion aragonite (Table 2).

Therefore, our hypothesis that growth by attachment of amorphous precursor particles confers the advantage of fast skeleton growth to corals seems to be confirmed by data: aragonite crystal growth via particle attachment in both synthetic spherulites and coral skeletons is more than 100 times faster than ion-by-ion growth from solution. This must be an advantage in the competitive and crowded reef environment. It also provides an avenue to fine-tune paleoclimate proxies using synthetic crystals grown by particle attachment. Coral bleaching (80) and postmortem skeleton dissolution (81) are increasingly occurring, but coral skeleton growth rate in S. pistillata will not necessarily be decreased by ocean acidification. Additional experiments on growth rates at lower pH will shed light on this possibility. If other corals also form their skeletons by particle attachment, a calcification crisis may or may not occur in acidifying oceans, because ACC particles are formed inside coral tissue.

Materials and Methods

Detailed methods are provided in *SI Materials and Methods*. Briefly, *S. pistillata* corals, adults and spats, were fixed, dehydrated, embedded, polished, and coated for PEEM analysis as described previously (23, 32). For confocal microscopy, they were exposed to blue calcein in seawater, washed, and observed alive, so that blue calcein particles could be imaged in the LT and in the forming biomineral. For PEEM experiments, sample preparations were rapid and repeated to capture the transforming amorphous phases; PEEM data acquisition was done exposing the sample to as little radiation damage as possible, which has the effect of crystallizing amorphous phases. Data processing was done using Ca L-edge component mapping with four spectral components (ACC-H_2O, ACC, pAra, and aragonite) after normalizing these spectra to have the same area under the whole spectrum between 345 and 355 eV. With this approach, quantitative analysis of the concentration of each component can be done, giving equal weight to crystalline and amorphous phases. This normalization differs from the ones used previously (23, 32).

Note Added in Proof. Two recently published articles are closely related to this work and strongly support it. Sun et al. (106) demonstrate that *S. pistillata* corals grow their skeletons spherulitically. Walker et al. (107) characterize in vitro a solid state transformation from ACC to aragonite similar to the biogenic one observed here.

Table 4. Abiotic aragonite particle-by-particle growth rate

Study	Synthetic spherulite linear growth rate (μm/d)
This study, range across 15 spherulites	14–60
Average of all growth rates ± SD	29 ± 12

Linear growth rate measured in this study in aragonite spherulites grown for 24 h by attachment of nanoparticles.

1. Allemand D, Tambutté É, Zoccola D, Tambutté S (2011) Coral calcification, cells to reefs. *Coral Reefs: An Ecosystem in Transition*, eds Dubinsky Z, Stambler N (Springer, Berlin), pp 119–150.
2. Tambutté S, et al. (2011) Coral biomineralization: From the gene to the environment. *J Exp Mar Biol Ecol* 408:58–78.
3. Davy SK, Allemand D, Weis VM (2012) Cell biology of cnidarian-dinoflagellate symbiosis. *Microbiol Mol Biol Rev* 76:229–261.
4. Constantz BR (1986) Coral skeleton construction; a physiochemically dominated process. *Palaios* 1:152–157.
5. Weiner S, Dove PM (2003) An overview of biomineralization processes and the problem of the vital effect. *Rev Mineral Geochem* 54:1–29.
6. Cohen AL, Owens KE, Layne GD, Shimizu N (2002) The effect of algal symbionts on the accuracy of Sr/Ca paleotemperatures from coral. *Science* 296:331–333.
7. Adkins JF, Boyle EA, Curry WB, Lutringer A (2003) Stable isotopes in deep-sea corals and a new mechanism for "vital effects." *Geochim Cosmochim Acta* 67:1129–1143.
8. Blamart D, et al. (2007) Correlation of boron isotopic composition with ultrastructure in the deep-sea coral Lophelia pertusa: Implications for biomineralization and paleo-pH. *Geochem Geophys Geosyst* 8:1–11.
9. Vidavsky N, et al. (2016) Calcium transport into the cells of the sea urchin larva in relation to spicule formation. *Proc Natl Acad Sci USA* 113:12637–12642.
10. Lowenstam HA, Weiner S (1989) *On Biomineralization* (Oxford Univ Press, Oxford).
11. Beck JW, et al. (1992) Sea-surface temperature from coral skeletal strontium/calcium ratios. *Science* 257:644–647.
12. Zachos JC, et al. (2005) Rapid acidification of the ocean during the Paleocene-Eocene thermal maximum. *Science* 308:1611–1615.
13. Gothmann AM, et al. (2015) Fossil corals as an archive of secular variations in seawater chemistry since the Mesozoic. *Geochim Cosmochim Acta* 160:188–208.
14. Anthony KR, Kline DI, Diaz-Pulido G, Dove S, Hoegh-Guldberg O (2008) Ocean acidification causes bleaching and productivity loss in coral reef builders. *Proc Natl Acad Sci USA* 105:17442–17446.
15. Pearse VB (1970) Incorporation of CO₂ into coral skeleton. *Nature* 228:383–383.
16. Raz-Bahat M, Erez J, Rinkevich B (2006) In vivo light-microscopic documentation for primary calcification processes in the hermatypic coral *Stylophora pistillata*. *Cell Tissue Res* 325:361–368.
17. Cohen AL, McConnaughey TA (2003) Geochemical perspectives on coral mineralization. *Rev Mineral Geochem* 54:151–187.
18. Clode PL, Lema K, Saunders M, Weiner S (2011) Skeletal mineralogy of newly settling *Acropora millepora* (Scleractinia) coral recruits. *Coral Reefs* 30:1–8.
19. Stolarski J (2003) Three-dimensional micro-and nanostructural characteristics of the scleractinian coral skeleton: A biocalcification proxy. *Acta Palaeontol Pol* 48:497–530.
20. Mass T, Drake JL, Peters EC, Jiang W, Falkowski PG (2014) Immunolocalization of skeletal matrix proteins in tissue and mineral of the coral Stylophora pistillata. *Proc Natl Acad Sci USA* 111:12728–12733.
21. Gal A, et al. (2014) Particle accretion mechanism underlies biological crystal growth from an amorphous precursor phase. *Adv Funct Mater* 24:5420–5426.
22. De Yoreo JJ, et al. (2015) Crystallization by particle attachment in synthetic, biogenic, and geologic environments. *Science* 349:aaa6760.
23. DeVol RT, et al. (2015) Nanoscale transforming mineral phases in fresh nacre. *J Am Chem Soc* 137:13325–13333.
24. Pokroy B, et al. (2015) Narrowly distributed crystal orientation in biomineral vaterite. *Chem Mater* 27:6516–6523.
25. Meibom A, et al. (2004) Distribution of magnesium in coral skeleton. *Geophys Res Lett* 31:1–4.
26. Reggi M, et al. (2014) Biomineralization in mediterranean corals: The role of the intraskeletal organic matrix. *Cryst Growth Des* 14:4310–4320.
27. Falini G, Fermani S, Goffredo S (2015) Coral biomineralization: A focus on intra-skeletal organic matrix and calcification. *Semin Cell Dev Biol* 46:17–26.
28. Beniash E, Aizenberg J, Addadi L, Weiner S (1997) Amorphous calcium carbonate transforms into calcite during sea urchin larval spicule growth. *Proc R Soc Lond B Biol Sci* 264:461–465.
29. Politi Y, Arad T, Klein E, Weiner S, Addadi L (2004) Sea urchin spine calcite forms via a transient amorphous calcium carbonate phase. *Science* 306:1161–1164.
30. Weiss IM, Tuross N, Addadi L, Weiner S (2002) Mollusc larval shell formation: Amorphous calcium carbonate is a precursor phase for aragonite. *J Exp Zool* 293:478–491.
31. Politi Y, et al. (2008) Transformation mechanism of amorphous calcium carbonate into calcite in the sea urchin larval spicule. *Proc Natl Acad Sci USA* 105:17362–17366.
32. Gong YUT, et al. (2012) Phase transitions in biogenic amorphous calcium carbonate. *Proc Natl Acad Sci USA* 109:6088–6093.
33. Radha AV, Forbes TZ, Killian CE, Gilbert PUPA, Navrotsky A (2010) Transformation and crystallization energetics of synthetic and biogenic amorphous calcium carbonate. *Proc Natl Acad Sci USA* 107:16438–16443.
34. Metzler RA, Tribello GA, Parrinello M, Gilbert PUPA (2010) Asprich peptides are occluded in calcite and permanently disorder biomineral crystals. *J Am Chem Soc* 132:11585–11591.
35. Cuif J-P, Dauphin Y, Doucet J, Salome M, Susini J (2003) XANES mapping of organic sulfate in three scleractinian coral skeletons. *Geochim Cosmochim Acta* 67:75–83.
36. Von Euw S, et al. (2017) Biological control of aragonite formation in stony corals. *Science* 356:933–938.
37. Cartwright JH, Checa AG, Gale JD, Gebauer D, Sainz-Díaz CI (2012) Calcium carbonate polyamorphism and its role in biomineralization: How many amorphous calcium carbonates are there? *Angew Chem Int Ed Engl* 51:11960–11970.
38. Farhadi-Khouzani M, Chevrier DM, Zhang P, Hedin N, Gebauer D (2016) Water as the key to proto-aragonite amorphous CaCO3. *Angew Chem Int Ed Engl* 55:8117–8120.
39. Killian CE, et al. (2009) Mechanism of calcite co-orientation in the sea urchin tooth. *J Am Chem Soc* 131:18404–18409.
40. DeVol RT, et al. (2014) Oxygen spectroscopy and polarization-dependent imaging contrast (PIC)-mapping of calcium carbonate minerals and biominerals. *J Phys Chem B* 118:8449–8457.
41. Gilbert PUPA, Young A, Coppersmith SN (2011) Measurement of c-axis angular orientation in calcite (CaCO₃) nanocrystals using X-ray absorption spectroscopy. *Proc Natl Acad Sci USA* 108:11350–11355.
42. Venn A, Tambutté E, Holcomb M, Allemand D, Tambutté S (2011) Live tissue imaging shows reef corals elevate pH under their calcifying tissue relative to seawater. *PLoS One* 6:e20013.
43. Clode PL, Marshall AT (2002) Low temperature FESEM of the calcifying interface of a scleractinian coral. *Tissue Cell* 34:187–198.
44. Gilis M, et al. (2014) Biomineralization in newly settled recruits of the scleractinian coral Pocillopora damicornis. *J Morphol* 275:1349–1365.
45. Erez J, Braun A (2007) Calcification in hermatypic corals is based on direct seawater supply to the biomineralization site. *Geochim Cosmochim Acta* 71(15 Suppl 1):A260.
46. Tambutté E, et al. (2012) Calcein labelling and electrophysiology: Insights on coral tissue permeability and calcification. *Proc Biol Sci* 279:19–27.
47. Khalifa GM, et al. (2016) Biomineralization pathways in a foraminifer revealed using a novel correlative cryo-fluorescence-SEM-EDS technique. *J Struct Biol* 196:155–163.
48. Tambutté E, et al. (2007) Observations of the tissue-skeleton interface in the scleractinian coral Stylophora pistillata. *Coral Reefs* 26:517–529.
49. Schauer KL, et al. (2016) A proteinaceous organic matrix regulates carbonate mineral production in the marine teleost intestine. *Sci Rep* 6:34494.
50. Zoccola D, et al. (2015) Bicarbonate transporters in corals point towards a key step in the evolution of cnidarian calcification. *Sci Rep* 5:9983.
51. Comeau S, et al. (2017) Coral calcifying fluid pH is modulated by seawater carbonate chemistry not solely seawater pH. *Proc Biol Sci* 284:20161669.
52. Vidavsky N, Masic A, Schertel A, Weiner S, Addadi L (2015) Mineral-bearing vesicle transport in sea urchin embryos. *J Struct Biol* 192:358–365.
53. Vidavsky N, et al. (2014) Initial stages of calcium uptake and mineral deposition in sea urchin embryos. *Proc Natl Acad Sci USA* 111:39–44.
54. Yang L, Killian CE, Kunz M, Tamura N, Gilbert PUPA (2011) Biomineral nanoparticles are space-filling. *Nanoscale* 3:603–609.
55. Schrag DP, Linsley BK (2002) Paleoclimate. Corals, chemistry, and climate. *Science* 296:277–278.
56. Saenger C, Erez J (2016) A non-traditional stable isotope perspective on coral calcification. *The Cnidaria, Past, Present and Future*, eds Goffredo S, Dubinsky Z (Springer, Berlin), pp 181–205.
57. Lobel PS (2001) Kinetic control of skeletal Sr/Ca in a symbiotic coral: Implications for the paleotemperature proxy. *Paleoceanography* 16:20–26.
58. Hönisch B, et al. (2012) The geological record of ocean acidification. *Science* 335:1058–1063.
59. Gagnon AC, Adkins JF, Fernandez DP, Robinson LF (2007) Sr/Ca and Mg/Ca vital effects correlated with skeletal architecture in a scleractinian deep-sea coral and the role of Rayleigh fractionation. *Earth Planet Sci Lett* 261:280–295.
60. Gaetani GA, Cohen AL (2006) Element partitioning during precipitation of aragonite from seawater: A framework for understanding paleoproxies. *Geochim Cosmochim Acta* 70:4617–4634.
61. Gagnon AC, Adkins JF, Erez J (2012) Seawater transport during coral biomineralization. *Earth Planet Sci Lett* 329:150–161.
62. Urey HC, Lowenstam HA, Epstein S, McKinney CR (1951) Measurement of paleo-temperatures and temperatures of the upper cretaceous of England, Denmark, and the southeastern United States. *Geol Soc Am Bull* 62:399–416.
63. Spero HJ, Bijma J, Lea DW, Bemis BE (1997) Effect of seawater carbonate concentration on foraminiferal carbon and oxygen isotopes. *Nature* 390:497–500.
64. Bertucci A, Tambutté S, Supuran CT, Allemand D, Zoccola D (2011) A new coral carbonic anhydrase in *Stylophora pistillata*. *Mar Biotechnol (NY)* 13:992–1002.
65. Venn AA, et al. (2009) Imaging intracellular pH in a reef coral and symbiotic anemone. *Proc Natl Acad Sci USA* 106:16574–16579.

66. Tambutte E, Allemand D, Mueller E, Jaubert J (1996) A compartmental approach to the mechanism of calcification in hermatypic corals. *J Exp Biol* 199:1029–1041.

67. Bhattacharya D, et al. (2016) Comparative genomics explains the evolutionary success of reef-forming corals. *eLife* 5:e13288.

68. Ghosh P, et al. (2006) 13 C–18 O bonds in carbonate minerals: A new kind of paleothermometer. *Geochim Cosmochim Acta* 70:1439–1456.

69. Stephenson AE, et al. (2008) Peptides enhance magnesium signature in calcite: Insights into origins of vital effects. *Science* 322:724–727.

70. Stoll HM, Schrag DP (2000) Coccolith Sr/Ca as a new indicator of coccolithophorid calcification and growth rate. *Geochem Geophys Geosyst* 1:1–24.

71. Lea DW, Mashiotta TA, Spero HJ (1999) Controls on magnesium and strontium uptake in planktonic foraminifera determined by live culturing. *Geochim Cosmochim Acta* 63:2369–2379.

72. Van Santen R (1984) The Ostwald step rule. *J Phys Chem* 88:5768–5769.

73. Navrotsky A (2004) Energetic clues to pathways to biomineralization: Precursors, clusters, and nanoparticles. *Proc Natl Acad Sci USA* 101:12096–12101.

74. Penn RL, Banfield JF (1999) Morphology development and crystal growth in nanocrystalline aggregates under hydrothermal conditions: Insights from titania. *Geochim Cosmochim Acta* 63:1549–1557.

75. Banfield JF, Welch SA, Zhang H, Ebert TT, Penn RL (2000) Aggregation-based crystal growth and microstructure development in natural iron oxyhydroxide biomineralization products. *Science* 289:751–754.

76. Cölfen H, Antonietti M (2005) Mesocrystals: Inorganic superstructures made by highly parallel crystallization and controlled alignment. *Angew Chem Int Ed Engl* 44: 5576–5591.

77. Cölfen H, Antonietti M (2008) *Mesocrystals and Nonclassical Crystallization* (Wiley, New York).

78. De'ath G, Fabricius KE, Sweatman H, Puotinen M (2012) The 27-year decline of coral cover on the great barrier reef and its causes. *Proc Natl Acad Sci USA* 109: 17995–17999.

79. Rosenfeld M, Yam R, Shemesh A, Loya Y (2003) Implication of water depth on stable isotope composition and skeletal density banding patterns in a Porites lutea colony: Results from a long-term translocation experiment. *Coral Reefs* 22:337–345.

80. Hughes TP, et al. (2017) Global warming and recurrent mass bleaching of corals. *Nature* 543:373–377.

81. Orr JC, et al. (2005) Anthropogenic ocean acidification over the twenty-first century and its impact on calcifying organisms. *Nature* 437:681–686.

82. Burton EA, Walter LM (1987) Relative precipitation rates of aragonite and Mg calcite from seawater: Temperature or carbonate ion control? *Geology* 15:111–114.

83. Mucci A, Canuel R, Zhong S (1989) The solubility of calcite and aragonite in sulfate-free seawater and the seeded growth kinetics and composition of the precipitates at 25 C. *Chem Geol* 74:309–320.

84. Zhong S, Mucci A (1989) Calcite and aragonite precipitation from seawater solutions of various salinities: Precipitation rates and overgrowth compositions. *Chem Geol* 78: 283–299.

85. Gutjahr A, Dabringhaus H, Lacmann R (1996) Studies of the growth and dissolution kinetics of the $CaCO_3$ polymorphs calcite and aragonite I. Growth and dissolution rates in water. *J Cryst Growth* 158:296–309.

86. Liberman T, Genin A, Loya Y (1995) Effects on growth and reproduction of the coral Stylophora pistillata by the mutualistic damselfish Dascyllus marginatus. *Mar Biol* 121:741–746.

87. Kotb MM (2001) Growth rates of three reef-building coral species in the northern Red Sea, Egypt. *Egypt J Aquat Biol Fish* 5:165–185.

88. Shaish L, Abelson A, Rinkevich B (2006) Branch to colony trajectory in a modular organism: Pattern formation in the Indo-Pacific coral Stylophora pistillata. *Dev Dyn* 235:2111–2121.

89. Nancollas G, Reddy M (1971) The crystallization of calcium carbonate. II. Calcite growth mechanism. *J Colloid Interface Sci* 37:824–830.

90. Mucci A, Morse JW (1983) The incorporation of Mg^{2+} and Sr^{2+} into calcite overgrowths: Influences of growth rate and solution composition. *Geochim Cosmochim Acta* 47:217–233.

91. Morse JW, Mucci A, Millero FJ (1980) The solubility of calcite and aragonite in seawater of 35%. salinity at 25 C and atmospheric pressure. *Geochim Cosmochim Acta* 44:85–94.

92. Millero FJ, Feistel R, Wright DG, McDougall TJ (2008) The composition of standard seawater and the definition of the reference-composition salinity scale. *Deep Sea Res Part 1 Oceanogr Res Pap* 55:50–72.

93. Bongiorni L, Shafir S, Rinkevich B (2003) Effects of particulate matter released by a fish farm (Eilat, Red Sea) on survival and growth of Stylophora pistillata coral nubbins. *Mar Pollut Bull* 46:1120–1124.

94. Mass T, et al. (2007) Photoacclimation of Stylophora pistillata to light extremes: Metabolism and calcification. *Mar Ecol Prog Ser* 334:93–102.

95. Moya A, et al. (2006) Study of calcification during a daily cycle of the coral Stylophora pistillata: Implications for 'light-enhanced calcification'. *J Exp Biol* 209:3413–3419.

96. Gilbert PUPA (2014) Photoemission spectromicroscopy for the biomineralogist. *Biomineralization Sourcebook, Characterization of Biominerals and Biomimetic Materials*, eds DiMasi E, Gower LB (CRC, Boca Raton, FL), pp 135–151.

97. Frazer BH, Gilbert B, Sonderegger BR, De Stasio G (2003) The probing depth of total electron yield in the sub keV range: TEY-XAS and X-PEEM. *Surf Sci* 537:161–167.

98. De Stasio G, Frazer BH, Gilbert B, Richter KL, Valley JW (2003) Compensation of charging in X-PEEM: A successful test on mineral inclusions in 4.4 Ga old zircon. *Ultramicroscopy* 98:57–62.

99. Falini G, Albeck S, Weiner S, Addadi L (1996) Control of aragonite or calcite polymorphism by mollusk shell macromolecules. *Science* 271:67–69.

100. GG Macros (2017) Available at home.physics.wisc.edu/gilbert/software. Accessed August 10, 2017.

101. Metzler RA, et al. (2007) Architecture of columnar nacre, and implications for its formation mechanism. *Phys Rev Lett* 98:268102.

102. Metzler RA, et al. (2008) Polarization-dependent imaging contrast in abalone shells. *Phys Rev B* 77:064110.

103. Olson IC, Kozdon R, Valley JW, Gilbert PUPA (2012) Mollusk shell nacre ultrastructure correlates with environmental temperature and pressure. *J Am Chem Soc* 134: 7351–7358.

104. Olson IC, et al. (2013) Crystal nucleation and near-epitaxial growth in nacre. *J Struct Biol* 184:454–463.

105. Press WH, Teukolsky SA, Vetterling WT, Flannery BP (1992) *Numerical Recipes in Fortran* (Cambridge Univ Press, Cambridge, UK).

106. Sun CY, et al. (2017) Spherulitic growth of coral skeletons and synthetic aragonite: Nature's three-dimensional printing. *ACS Nano* 11:6612–6622.

107. Walker JM, Marzec B, Nudelman F (July 25, 2017) Solid–state transformation of amorphous calcium carbonate to aragonite captured by cryoTEM. *Angew Chem Int Ed Engl*, 10.1002/anie.201703158.